The Effects of Wind Forcing and Background Mean Currents on the Latitudinal Structure of Equatorial Rossby Waves

RENELLYS C. PEREZ, DUDLEY B. CHELTON, AND ROBERT N. MILLER

College of Oceanic and Atmospheric Sciences, Oregon State University, Corvallis, Oregon

ABSTRACT

The latitudinal structure of annual equatorial Rossby waves in the tropical Pacific Ocean based on sea surface height (SSH) and thermocline depth observations is equatorially asymmetric, which differs from the structure of the linear waves of classical theory that are often presumed to dominate the variability. The nature of this asymmetry is such that the northern SSH maximum (along 5.5°N) is roughly 2 times that of the southern maximum (along 6.5°S). In addition, the observed westward phase speeds are roughly 0.5 times the predicted speed of 90 cm s^{-1} and are also asymmetric with the northern phase speeds, about 25% faster than the southern phase speeds. One hypothesized mechanism for the observed annual equatorial Rossby wave amplitude asymmetry is modification of the meridional structure by the asymmetric meridional shears associated with the equatorial current system. Another hypothesis is the asymmetry of the annually varying wind forcing, which is stronger north of the equator. A reduced-gravity, nonlinear, β-plane model with rectangular basin geometry forced by idealized Quick Scatterometer (QuikSCAT) wind stress is used to test these two mechanisms. The model with an asymmetric background mean current system perturbed with symmetric annually varying winds consistently produces asymmetric Rossby waves with a northern maximum (4.7°N) that is 1.6 times the southern maximum (5.2°S) and westward phase speeds of approximately 53 ± 13 cm s^{-1} along both latitudes. Simulations with a symmetric background mean current system perturbed by asymmetric annually varying winds fail to produce the observed Rossby wave structure unless the perturbation winds become strong enough for nonlinear interactions to produce asymmetry in the background mean current system. The observed latitudinal asymmetry of the phase speed is found to be critically dependent on the inclusion of realistic coastline boundaries.

1. Introduction

Sea surface height (SSH) and thermocline depth observations of equatorial Rossby waves in the Pacific Ocean consistently show asymmetric latitudinal structure in the equatorial waveguide (Chelton et al. 2003 and references therein). It is often presumed that the vertical mode-1, meridional mode-1 Rossby waves of classical theory in which zero background mean flow is assumed (Matsuno 1966; Moore 1968; Moore and Philander 1977) dominate the seasonal to interannual variability in the tropical Pacific. The observed equatorial Rossby wave structure, however, differs from the symmetric structure of the baroclinic, meridional mode-1 Rossby waves. Baroclinic gravity wave speeds c_1 based on hydrographic data (e.g., Eriksen et al. 1983; Chelton et al. 1998) in the equatorial Pacific range from 2.3 m s^{-1} near the Galapagos Islands to 3.0 m s^{-1} near

the date line (Eriksen et al. 1983) and the western boundary currents (Chelton et al. 1998). Given a characteristic c_1 of about 2.6 m s^{-1}, the first meridional mode for SSH has symmetric local maxima along 3.7°N and 3.7°S and a local minimum along the equator (solid line, Fig. 1). The observed maxima, however, are located along higher latitudes than this and are asymmetric with larger amplitude north of the equator. Classical theory also predicts a phase speed of 90 cm s^{-1}, whereas the estimated phase speeds from observations are 30%–50% slower. The primary objective of this paper is to simulate the latitudinal structure of equatorial Rossby waves in the Pacific Ocean with a series of numerical experiments designed to investigate the mechanism for the mismatch between the observed and theoretical structure. We also investigate some aspects of the discrepancies between the observed and theoretical phase speeds.

The asymmetric latitudinal structure of equatorial Rossby waves has been documented from subsurface thermal data (Meyers 1979; Lukas and Firing 1985; Kessler 1990; Kessler and McCreary 1993; Yu and McPhaden 1999) and from altimeter data (Delcroix et al. 1991; Fu et al. 1991; Delcroix et al. 1994; Susanto et

Corresponding author address: Renellys C. Perez, College of Oceanic and Atmospheric Sciences, Oregon State University, 104 Ocean Administration Building, Corvallis, OR 97331.
E-mail: rperez@coas.oregonstate.edu
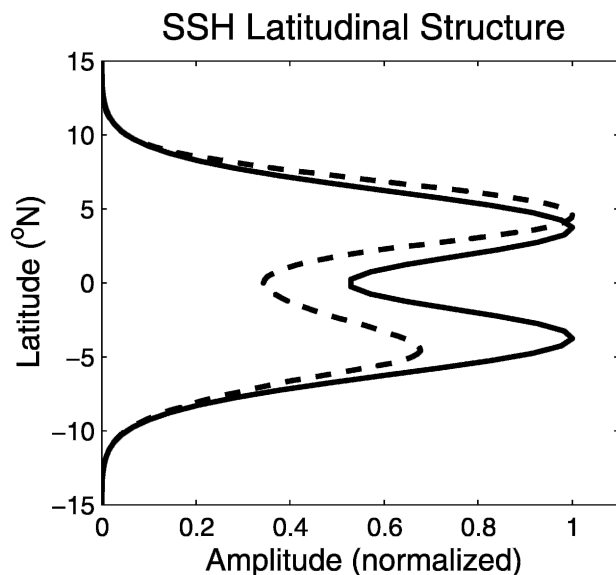
SSH Latitudinal Structure

FIG. 1. Latitudinal structure function for SSH meridional mode-1, vertical mode-1 Rossby waves as predicted by classical theory (solid line) and by the shear-modified theory (dashed line) of Chelton et al. (2003).

al. 1998). The most recent analysis by Chelton et al. (2003) from 8.5 yr of Ocean Topography Experiment (TOPEX)/Poseidon measurements of SSH provides a thorough description of the latitudinally asymmetric structure of broadbanded Rossby waves. The observed local maxima along 5.5°N are roughly 2 times those along 5.5°S. The same asymmetry is observed when the annual cycle amplitude and phase are isolated during August 1999–July 2001 in the TOPEX/Poseidon dataset (Fig. 2). This asymmetric latitudinal structure is maintained over much of the Pacific basin, with only small zonal variations (upper-left panel, Fig. 2). The northern maximum along 5.5°N as determined by a zonal average between 170° and 240°E is 1.8 times the southern maximum along 6.5°S (upper-right panel, Fig. 2) and the estimated westward phase speeds of annual Rossby waves along these latitudes are 55.0 ± 14.2 and 43.3 ± 6.8 cm s^{-1}, respectively (see section 2c for methodology). Within the uncertainties of these estimates, these phase speeds of annual variability are consistent with the latitudinally asymmetric phase speed estimates obtained by Chelton et al. (2003) from broadbanded variability.

Various hypotheses have been put forth to explain the observed equatorial asymmetry, including superposition of meridional Rossby wave modes, asymmetries in the time-varying wind forcing, and asymmetries in the background mean currents (cf. section 2 of Chelton et al. 2003). Since each meridional mode has a corresponding phase speed that is inversely proportional to the mode number, it is unlikely that a superposition of more than one meridional mode could produce the observed asymmetric latitudinal structure across the large zonal distance over which it is observed. A modeling

study by Kessler and McCreary (1993) suggests that asymmetric time-varying wind forcing of a linear model with zero mean background currents also cannot produce latitudinally asymmetric Rossby waves.

From consideration of the eigensolutions of a simple 1.5-layer, unforced equatorial β-plane model linearized about a symmetric Equatorial Undercurrent (EUC), Philander (1979) showed that the Rossby wave maxima shift to higher latitudes, but the influence of the complete equatorial current system (ECS) on the structure of the waves was not analyzed in that study. Chelton et al. (2003) linearized the same model about the observed mean currents along seven longitudes in the Pacific and concluded that meridional shears in the background currents and associated modification of the meridional potential vorticity gradient are sufficient to generate asymmetric Rossby wave amplitudes (dashed line, Fig. 1) and reduce the westward phase speeds by 20% (71 cm s^{-1}). The slower westward phase speeds in the presence of equatorially asymmetric background shear had previously been documented from eigensolutions for an idealized mean ECS by Chang and Philander (1989) and Zheng et al. (1994). The effects of the background shear on the latitudinal structure of the eigenfunctions were not considered in these earlier studies.

In this study, we investigate numerically the importance of wind forcing and background currents in explaining the observed equatorial Rossby wave asymmetry. In section 2, the numerical model, wind forcing, and methodology of the hypothesis tests are detailed. A benchmark model run is compared with available satellite altimetry data in section 3. We perform a series of model runs detailed in sections 4 and 5 to investigate whether the observed asymmetry of the Rossby waves is due to asymmetry of the background mean currents or to asymmetry of the time-varying wind forcing. Since the background mean flow of the ECS is created by the asymmetric mean forcing of the northeast and southeast trades, it is a challenge to distinguish between these two hypotheses. For the present discussion, we evaluate whether either source is individually sufficient to generate the observed Rossby wave asymmetry. In section 4, the Rossby waves forced by symmetric annual cycle perturbation winds are analyzed in the presence of asymmetric mean currents set up by steady, asymmetric wind forcing. Conversely, section 5 analyzes the structure of Rossby waves forced by asymmetric annual cycle perturbation winds in the presence of symmetric currents set up by steady, symmetric wind forcing. By changing the magnitude of the perturbation winds relative to the background mean winds, we test the linearity of the system response and possible scales at which the perturbation begins to alter the background mean currents significantly. To quantify the subsurface effects of asymmetric currents on the Rossby waves, vertical structure and the modal decompositions of the model zonal velocity are also analyzed in section 4. The results
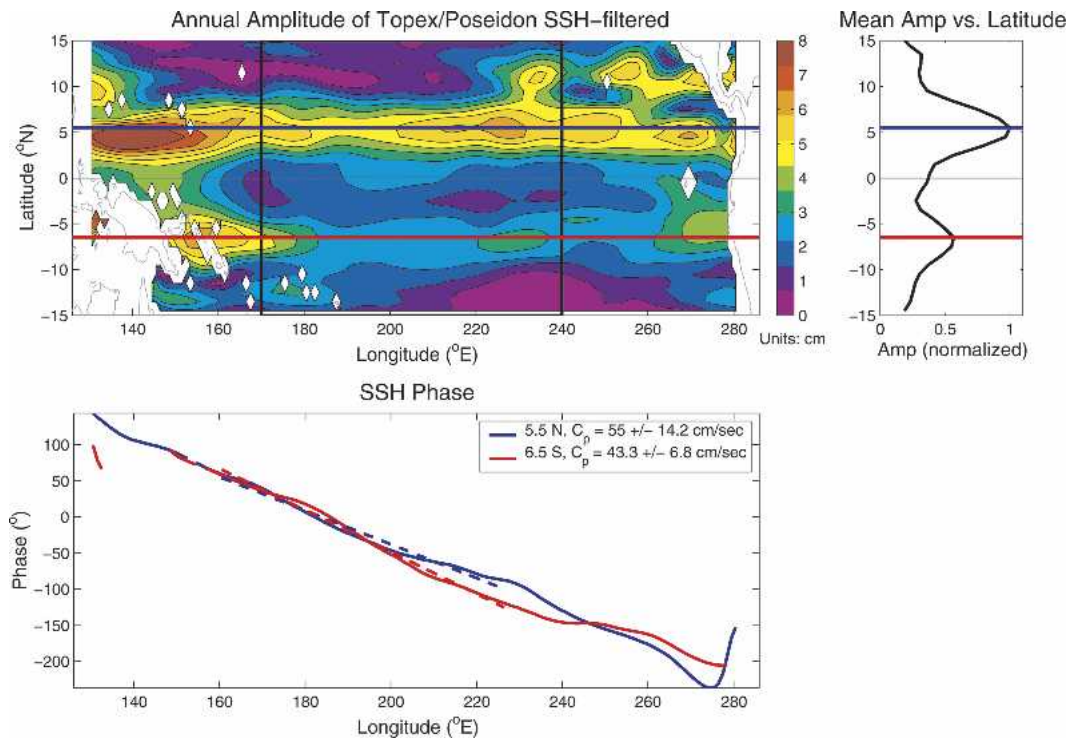
FIG. 2. SSH from Aug 1999 to Jul 2001 TOPEX/Poseidon measurements filtered to isolate Rossby wave signatures: (top left) SSH annual amplitude (cm), (top right) zonally averaged variability from 170° to 240°E, and (bottom) phase as a function of longitude along 6.5°S (red) and 5.5°N (blue).

of the numerical experiments and conclusions from the hypothesis tests are summarized in section 6.

2. The model as a hypothesis tester

a. Gent–Cane model

The Gent and Cane (1989) reduced-gravity, nonlinear, β-plane model (hereinafter the Gent–Cane model) and its evolution over the past two decades have been extensively documented. The model in this study is similar to the version detailed in Chen et al. (1994a,b) with the inclusion of salinity, which was found to be important to tropical ocean dynamics and thermodynamics (Murtugudde and Busalacchi 1998). This model has demonstrated its ability to reproduce the annual cycle of SST, mixed layer depth, thermocline depth, and zonal currents at the Tropical Atmosphere–Ocean (TAO) moorings along 110°W (Kessler et al. 1998; Hackert et al. 2001). It has been used to evaluate wind stress products as forcing fields (Hackert et al. 2001), has been incorporated as a component of advanced data assimilation systems (Verron et al. 1999), and has been applied to study all three tropical ocean basins (Murtugudde et al. 1996, 2002, and references therein).

The model domain covers the entire longitudinal extent of the Pacific Ocean (126°–286°E) and ranges from 30°S to 30°N. The dynamical model is a reduced-gravity model with a uniform surface mixed layer above an active layer divided into six σ-like layers relative to the bottom of the subthermocline active region defined by $T_{\text{bottom}} = 11°\text{C}$ and $S_{\text{bottom}} = 34.5$ psu (nominally at 400 m). Increased resolution of the subthermocline ocean can be achieved by changing the number of layers (NZ), bottom temperature, and salinity as in Hackert et al. (2001) where NZ = 20, $T_{\text{bottom}} = 6°\text{C}$, and $S_{\text{bottom}} = 35$ psu for tropical Pacific simulations. Along the equator, the simulated variability above the thermocline (the thermocline mean depth ranged from approximately 150 m at 140°E to 50 m at 95°W) is not notably stronger than TAO (Hackert et al. 2001).

The dynamic variables of the model are zonal velocity, meridional velocity, layer thickness, salinity, and temperature (u, v, h, S, T). At each hourly time step, these fields are calculated at 80×60 horizontal grid points, 3810 of which are ocean grid points when Pacific basin coastlines are included. The stretched horizontal grid has highest meridional resolution ($\sim 0.6°$) in the equatorial waveguide and gradually stretches to 3.3° at 30° latitude. The highest zonal resolution ($\sim 0.8°$) is located at the eastern and western boundaries with 2.4° resolution in the model interior. A hybrid mixing scheme designed by Chen et al. (1994a), which defines the dynamics of the surface mixed layer and allows for entrainment or detrainment between the layers, com-

TABLE 1. Parameter choices for different numerical experiments.

Parameter	Benchmark	Hypothesis 1	Hypothesis 2
Background wind	$(\bar{\tau}^x, \bar{\tau}^y)$	AS[a] $(\bar{\tau}^x, 0)$	SS[b] $(\bar{\tau}_s^x, 0)$
Perturbation wind	Seasonal cycle, asymmetric $\varepsilon = 1$	Annual cycle, symmetric $0.01 \leq \varepsilon \leq 0.10$	Annual cycle, asymmetric $0.01 \leq \varepsilon \leq 0.10$
Surface heat flux	Seasonal cycle	AS[a]	SS[b]
Relaxation to Levitus	Seasonal cycle	AS[a]	SS[b]
Coastlines	Included[c]	Rectangular basin	Rectangular basin

[a] AS indicates asymmetric, smoothed, mean fields [e.g., (1) in section 4].
[b] SS indicates symmetric, smoothed, mean fields [e.g., (5) in section 5].
[c] See Fig. 5 for the coastline representation on the model grid between 15°S and 15°N.

bines the Kraus and Turner (1967) mixed layer model with the Price et al. (1986) dynamical instability model.

Table 1 summarizes the model parameters selected for the benchmark run presented in section 3 and each hypothesis test (see sections 4 and 5 for detailed descriptions). In all of the cases discussed in this paper, the nonlinear advection terms are retained. For all model runs, no-slip conditions are imposed at the zonal and meridional boundaries. Experiments with free-slip boundary conditions were performed and little difference was observed. Coastlines are retained for the benchmark run described in section 3. For the hypothesis tests (sections 4 and 5), coastlines are removed to avoid boundary-induced asymmetries. To avoid introducing additional asymmetric forcing to experiments where symmetric background currents are desired, heat flux and precipitation at the model boundaries are symmetrized as a function of latitude with respect to the equator as described in section 5.

b. Wind forcing and background mean currents

1) QuikSCAT wind forcing

The SeaWinds scatterometer aboard the Quick Scatterometer (QuikSCAT) satellite was launched 19 June 1999 (Freilich et al. 1994). The two years beginning in August 1999 are of particular interest in this study because they include the most recent La Niña event. La Niña conditions are characterized by anomalously strong trade winds and strong wind stress divergence and curl over the northern front of the equatorial Pacific cold tongue (Chelton et al. 2001), amplifying latitudinal asymmetries in the climatological average wind field and in the ECS.

For this study, QuikSCAT monthly mean wind stresses from August 1999 to July 2001 are binned onto a 1° × 1° grid. The wind stresses are smoothed zonally using a one-dimensional "loess" smoother (Schlax and Chelton 1992) with a half span of 10° longitude, which corresponds to a 5° longitude block average. QuikSCAT mean wind stress resolves the well-known features in the tropical wind field, including the northeast and southeast trade winds and the wind jets through gaps in the Sierra Madre (upper-left panel of Fig. 3). There is high variability over the intertropical convergence zone (ITCZ) near New Guinea and in the

western Pacific between 15° and 30°N (upper-right panel, Fig. 3). QuikSCAT winds capture an intense zonal band of divergence over the northern front of the cold tongue (lower-left panel, Fig. 3). This enhanced divergence near the equator is thought to be an important driver for equatorial upwelling (de Szoeke and Chelton 2005, unpublished manuscript). There is also positive wind stress curl just north of the equator (lower-right panel, Fig. 3), which is present in scatterometer wind products such as European Remote Sensing Satellite *ERS-1* and QuikSCAT but is weak or absent in coarser-resolution wind products such as the ones developed by The Florida State University (FSU), the National Centers for Environmental Prediction (NCEP), and the European Centre for Medium-Range Weather Forecasts (ECMWF; Kessler et al. 2003; Chelton 2005).

To force the benchmark model run summarized in section 3, we fit these wind stresses to an annual cycle and three higher harmonics to generate a "seasonal cycle" during La Niña conditions. This seasonal cycle differs from that which would be obtained from a longer data record. The La Niña conditions during the first 2 years of the QuikSCAT mission are advantageous for the present purposes because of the amplified asymmetry in the background wind forcing that is believed to play an essential role in the asymmetry of equatorial Rossby waves.

2) Background mean currents

The observed meridional structure of the mean (years 1985–2000) ECS along 140°W estimated from ADCP/CTD transects by Johnson et al. (2002) is shown in the upper-left panel of Fig. 4. There is an equatorial asymmetry in the meridional shear due to the eastward-flowing North Equatorial Countercurrent (NECC) adjacent to the westward-flowing northern branch of the South Equatorial Current (SECN).

The benchmark run with realistic coastlines and forced with the QuikSCAT seasonal cycle winds (section 3) reproduces the salient features of the mean EUC and the mean NECC–SECN shear (upper-right panel, Fig. 4). The model NECC and SEC are somewhat weak, however, and the SEC is lacking in detail. Forcing the model with the spatially varying, 2-yr mean
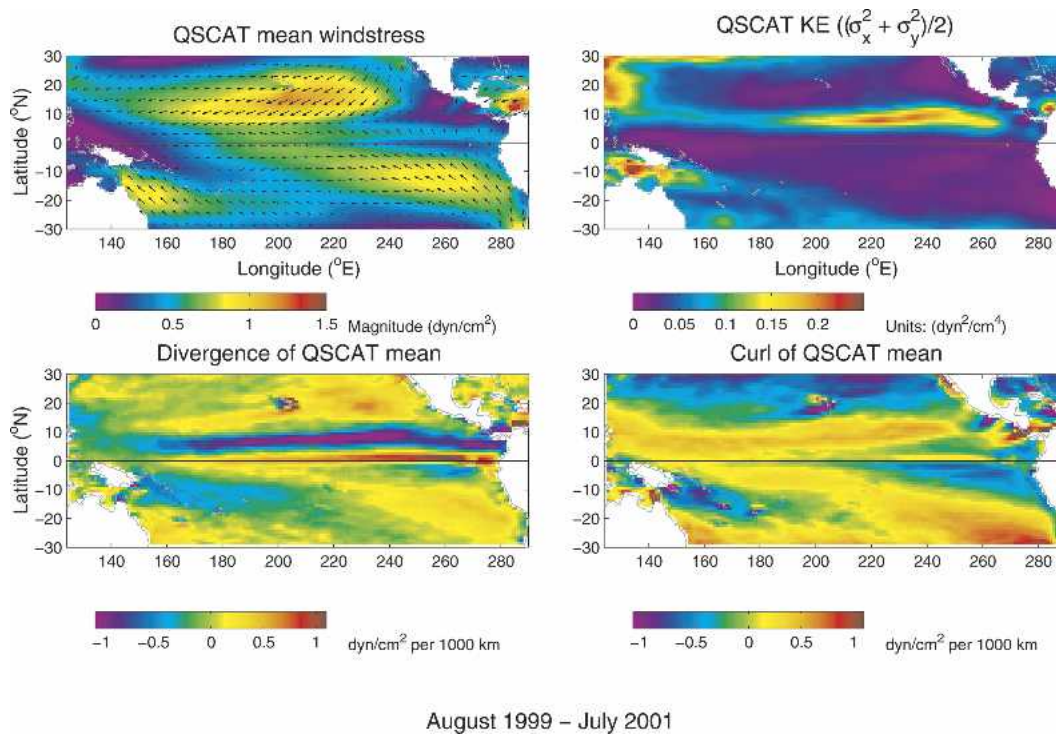
August 1999 – July 2001

FIG. 3. (top left) Mean, (top right) kinetic energy of the variance, (bottom left) divergence, and (bottom right) curl of QuikSCAT wind stress during Aug 1999–Jul 2001.

QuikSCAT wind stress (upper-left panel, Fig. 3) produces a mean NECC–SECN structure that appears similar to observations (lower-left panel, Fig. 4). The model mean EUC partially surfaces, however, and alters the sign of the simulated mixed layer currents at 141°W, producing larger meridional shears near the equator. This partial surfacing of the EUC is due to the lack of vertical shear within the surface mixed layer of the Gent–Cane model (Chen et al. 1994a). The background mean wind stress applied in the experiments
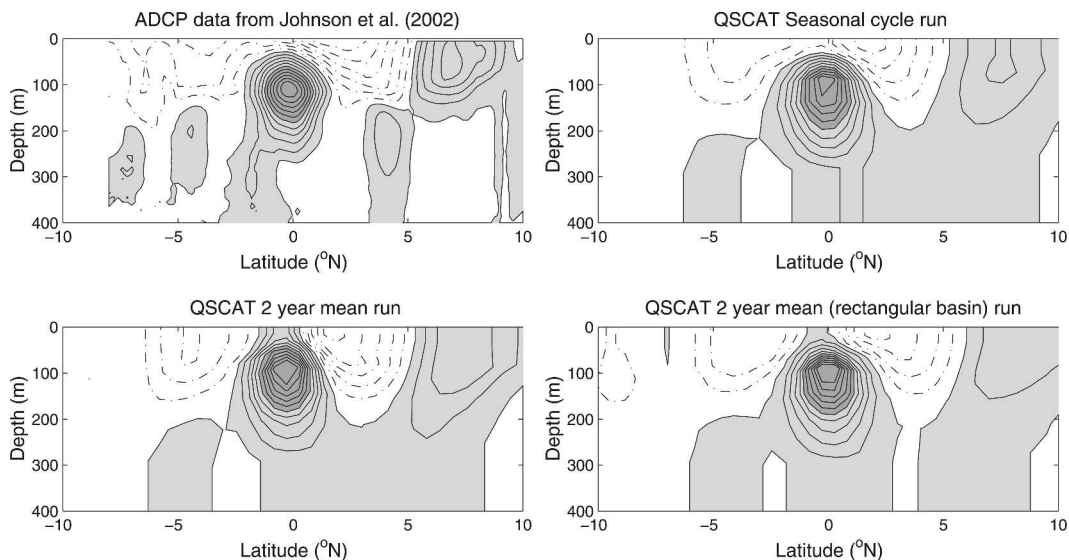

FIG. 4. (top left) ADCP mean zonal currents at 140°W from Johnson et al. (2002). Model background mean zonal currents at 141°W resulting from forcing with (top right) seasonal cycle QuikSCAT wind stress, (bottom left) QuikSCAT 2-yr mean wind stress, and (bottom right) QuikSCAT 2-yr mean zonal wind stress modified to a rectangular basin. Contour interval is 10 cm s^{-1}.

described in section 4 is a modified version of the 2-yr QuikSCAT mean and produces the mean zonal currents shown in the lower-right panel of Fig. 4.

The winds during the La Niña condition considered here produce a model ECS with stronger shear than during neutral or El Niño conditions. Despite the stronger forcing, we find that model meridional shears are somewhat weaker than those of the 15-yr mean zonal currents constructed from ADCP data by Johnson et al. (2002). Some of this discrepancy is due to aliasing of the ADCP data by tropical instability waves (TIWs), which result from the meridional and vertical shears in the ECS (Philander 1978; Cox 1980). Given this uncertainty, the meridional structure of the simulated ECS (lower-right panel of Fig. 4) will suffice to test the role of asymmetric mean currents in establishing the asymmetric latitudinal structure of equatorial Rossby waves (see section 4).

c. Extraction of the Rossby wave signal

The 5 years of model output analyzed for each simulation are stored as 3-day averages for each variable at all model locations. All of the model runs performed for this study generate TIWs with wave periods of about 35 days and zonal wavelengths of about 1600 km, which are consistent with the kinematic features of TIWs in numerous observational studies (e.g., Qiao and Weisberg 1995). The spatial and temporal resolution of the model is therefore sufficient to produce TIWs. Note that increased horizontal resolution in the Gent–Cane model increases the realism of the TIW statistics (Kessler et al. 1998).

To extract the Rossby wave signal for each experiment, the model SSH is filtered in a sequence of stages designed to mimic the processing applied by Chelton et al. (2003) to the satellite altimeter data. First, a zonal average across the full basin is removed from each grid location at each time step in an effort to eliminate the response from Ekman pumping with large zonal scales, thus isolating the propagating wave signals. A temporal low-pass filter is then applied to remove high-frequency processes, most notably Kelvin waves and the aforementioned TIWs. The low-pass filter consists of two passes of the data through a 150-day running mean. Last, an annual cycle is fit to the filtered SSH. The SSH Figs. 2, 5, 7, 11, and 14 in the sections that follow show the amplitude for the annual cycle regression between 15°S and 15°N and the phase along the northern and southern latitudes where the zonally averaged amplitudes are largest in the equatorial waveguide. The zonal wavelength λ is computed by fitting a straight line to the longitudinal variation of the annual phase (dashed lines in lower-left panels of the figures) and estimating the wavelength from the slope s by $\lambda = 2\pi\,s^{-1}$. Since the period (T) is annual, the westward phase speed estimate is just $|\lambda/T|$. The errors associated with these speeds are estimated by computing the phase speeds for smaller overlapping segments (30° zonal segments every 5° of longitude within the longitudinal range of the original straight line fit) and taking the standard deviation as the error bounds (Table 2).

TABLE 2. Westward phase speeds derived from observations, analytical theory, and Gent–Cane modeling experiments along latitudes of local SSH amplitude maxima.

Description	Lat (°S)	c_p (cm s^{-1})	Lat (°N)	c_p (cm s^{-1})
Classical theory ($m = 1$, $n = 1$)	3.7	90	3.7	90
Shear-modified theory ($m = 1$, $n = 1$)*	5.5	71	5.5	71
Broadband signal TOPEX/Poseidon*	5.5	48 ± 10	5.5	60 ± 15
Annual signal TOPEX/Poseidon	6.5	43.3 ± 6.8	5.5	55.0 ± 14.2
Benchmark Gent–Cane run	5.2	48.9 ± 3.4	5.2	55.4 ± 2.3
Hypothesis 1:				
$\varepsilon = 0.02$	5.2	53.4 ± 13.3	4.7	52.9 ± 13.3
$\varepsilon = 0.10$	5.2	51.8 ± 4.4	4.7	53.1 ± 12.7
Hypothesis 2:				
$\varepsilon = 0.02$	7.0	35.5 ± 6.0	6.4	39.4 ± 8.6
$\varepsilon = 0.10$	5.8	42.3 ± 9.5	5.2	45.0 ± 17.5

* Values from Chelton et al. (2003).

3. Benchmark run

The Gent–Cane model forced with the seasonal cycle QuikSCAT winds computed from 2 years of QuikSCAT [section 2b(1)] is able to simulate the salient features of the observed equatorial asymmetry with annual SSH amplitudes along 5.2°N more than 2 times those along 5.2°S (Fig. 5). East of 250°E along 5° and 10°N, there are patches of high SSH variability in both the TOPEX/Poseidon data and the benchmark run (Figs. 2 and 5, respectively), apparently due to local Ekman pumping in the lee of the Sierra Madre (Ducet et al. 2000; Kelly and Thompson 2002). While very similar in geographical structure, the model northern maximum is 25% weaker than the TOPEX/Poseidon maximum. In the central Pacific, a stronger latitudinal asymmetry is present in the benchmark run because of a weaker southern SSH maximum (Fig. 5). Simple kinematic arguments show that meridional shear in the mean zonal currents alters the meridional gradient of potential vorticity that sets up the amplitude of the Rossby waves. We find that the maxima in SSH amplitude are collocated with maxima in the meridional gradient of potential vorticity. The overall weaker southern maximum therefore results from the weaker meridional shear in the benchmark SEC in the central Pacific (upper-right panel of Fig. 4). Note that the combination of asymmetries in the mean and time-varying wind forcing used in the benchmark run may amplify the Rossby wave asymmetry in a way not readily explained by these simple kinematic arguments. The Rossby wave phase speeds along 5.2°N/S are similar to
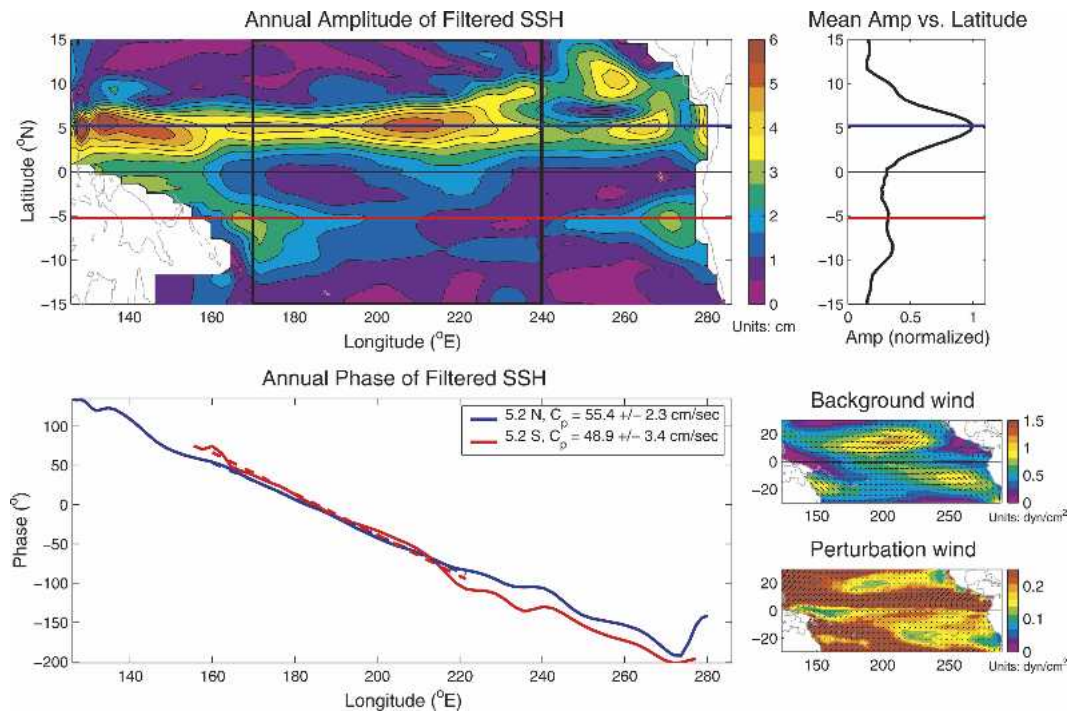
FIG. 5. SSH from the Gent–Cane model forced by seasonal QuikSCAT wind stress (benchmark run) and filtered to isolate Rossby wave signatures: (top left) SSH annual amplitude (cm), (top right) zonally averaged amplitude from 170° to 240°E, (bottom left) phase as a function of longitude along 5.2°S (red) and 5.2°N (blue), and (bottom right) structure of the steady (mean) wind and standard deviation of the perturbation wind stress (dyn cm^{-2}).

those estimated from observations with faster speeds in the north than in the south (55.4 ± 2.3 cm s^{-1} as compared with 48.9 ± 3.4 cm s^{-1}).

Depth-averaged (layers 4–7) zonal and meridional velocity annual amplitude (not shown) are in qualitative agreement with the geostrophic velocities estimated from altimeter measurements (Delcroix et al. 1994; Chelton et al. 2003). Layers 4–7 are chosen because they capture the modal structure in a more computationally stable fashion. The first empirical orthogonal functions (EOFs) for sea surface height and depth-averaged zonal and meridional velocity are plotted along six meridional transects as the thick solid lines in Fig. 6. The SSH EOF structures agree well with the first SSH EOFs from TOPEX/Poseidon data (thin solid lines) and the eigensolutions from 1.5-layer shear-modified theory (dashed lines) reproduced from Figs. 24 and 26 in Chelton et al. (2003). Although the simulated southern maximum is somewhat weak in the central Pacific in comparison with the observed and theoretical maxima, there is good agreement west of the date line. The structures of the zonal velocity EOF 1 also compare well to the observed and theoretical structures with the maximum shifted north of the equator by 1° to 2°. The meridional velocity comparisons are less clear, probably because the meridional velocity is so weak (generally <3 cm s^{-1}; see Fig. 13 of Chelton et al.

2003) and therefore difficult to isolate from noise. The locations of the northern maximum (near 4°N) and southern minimum (near 2°S) differ among the model, observations, and theory. The model meridional velocity has structure near the equator that cannot be validated with altimeter-based estimates as geostrophy fails near the equator. Except for the westernmost section, however, the latitudinal structure of meridional velocity near the equator in the model is quite similar to the eigensolutions of the 1.5-layer shear-modified theory.

Hydrographic observations in the tropical Pacific have found evidence of vertical Rossby wave propagation (Lukas and Firing 1985; Kessler and McCreary 1993). This raises the question of the suitability of the Gent–Cane model for Rossby wave process studies in the Tropics. The lack of downward energy flux associated with vertically propagating baroclinic Rossby waves [as in the modeling study of Dewitte and Reverdin (2000)] might be expected to trap energy in the upper ocean of the Gent–Cane model and produce anomalously large signals in the western Pacific. Neither is found to be the case here. Kessler and McCreary (1993) argued that resolving the low-frequency variations of the thermocline is sufficient to predict the subthermocline response to the wind forcing and that the vertical propagation they observed can be modeled with only a few baroclinic modes. The Gent–Cane
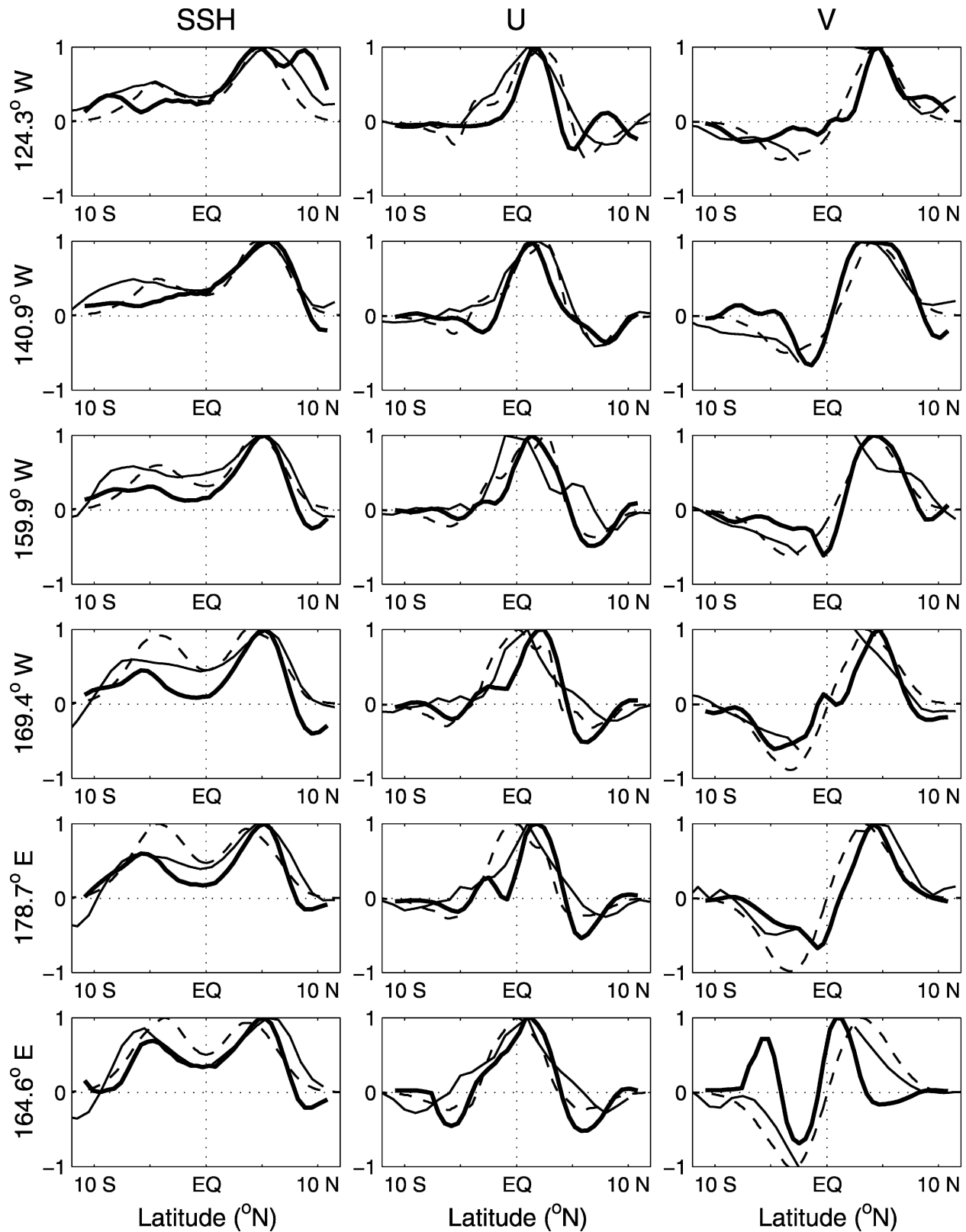
FIG. 6. First EOF of (left) SSH and depth-averaged (layers 4–7) (center) zonal and (right) meridional velocity along model transects nearest to (from top to bottom) 125°W, 140°W, 155°W, 170°W, 180°, and 165°E. The thick solid lines are EOF amplitudes computed from the benchmark run. TOPEX/Poseidon EOF amplitudes (thin solid lines) and the shear-modified theory eigensolutions (dashed lines) are from Chelton et al.'s (2003) Figs. 24 and 26.
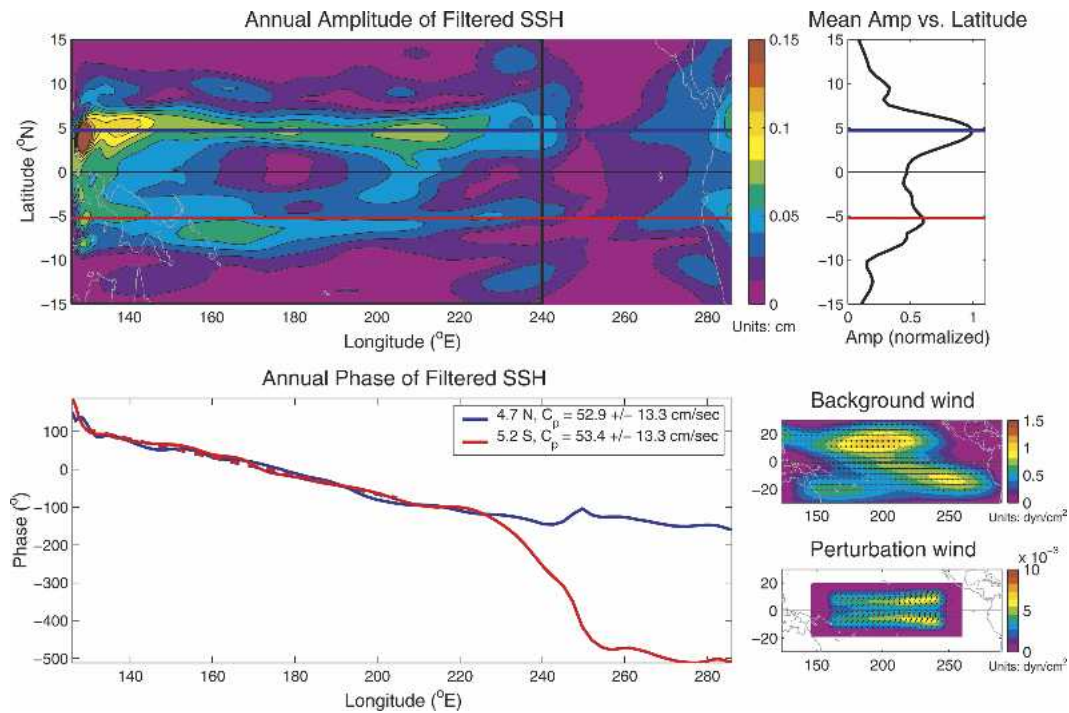
FIG. 7. Similar to Fig. 5, but SSH from the Gent–Cane model with a rectangular basin forced with 2-yr mean zonal wind plus symmetric perturbation winds ($\varepsilon = 0.02$) derived from QuikSCAT wind stress as described in the text. Zonally averaged amplitudes between 126° and 240°E. Phase lines along 5.2°S and 4.7°N are shown in red and blue, respectively.

model, which resolves the low-frequency variations of the thermocline (Hackert et al. 2001), reproduces the observed asymmetry of equatorial Rossby wave amplitudes and phase speeds in the benchmark run with acceptable realism. We therefore conclude that the Gent–Cane model is appropriate for testing hypotheses for the asymmetry of equatorial Rossby waves.

4. Hypothesis 1: Asymmetric background zonal currents

In the first set of experiments, we spun up the model with steady, equatorially asymmetric winds (a modification of the QuikSCAT 2-yr mean shown in Fig. 3) to obtain an asymmetric background mean ECS in a rectangular basin (lower-right panel, Fig. 4). The goal is to generate a latitudinally asymmetric mean circulation that possesses the general features of the Pacific Ocean (e.g., an equatorial Pacific cold tongue, warm pool, and NECC–SECN shear) without introducing boundary-induced asymmetry through coastline geometry.

The background meridional winds are set to zero everywhere for this set of experiments. Numerical experiments (not shown here) with nonzero mean meridional winds demonstrated that they do not significantly alter the symmetry of the eigensolutions or the phase speeds of the Rossby waves. The background wind field for the rectangular ocean basin considered here is generated

by bilinearly interpolating the 2-yr mean QuikSCAT zonal wind stress over the continents and setting the interpolated mean zonal wind stress to zero over the Gulf of Mexico and surrounding coastlines. The interpolated mean zonal wind stress is then smoothed to further reduce spurious winds over land boundaries by fitting at each latitude a low-order Fourier representation (two harmonics of the basin width X_E) of the form

$$\overline{\tau}^x(x, y) = a_0(y) + a_1(y) \cos\left(\frac{\pi x}{X_E}\right) + a_2(y) \sin\left(\frac{\pi x}{X_E}\right)$$

$$+ a_3(y) \cos\left(\frac{2\pi x}{X_E}\right) + a_4(y) \sin\left(\frac{2\pi x}{X_E}\right). \quad (1)$$

From comparison of the lower-right panel of Figs. 5 and 7, this fit captures the general features of the mean tropical Pacific winds.

Constant in time but spatially varying precipitation and heat flux forcing are applied at the surface to avoid introducing buoyancy-forced temporal variability. The mean surface heat flux is computed via the bulk formula of Seager et al. (1988) based on the mean cloud coverage from the International Satellite Cloud Climatology Project climatology (Rossow and Schiffer 1991), the mean wind speed, and constant solar fluxes. Following Chen et al. (1994a,b), the model solutions away from the equatorial region are restored to a Levitus (1982) mean state (h, S, and T) in a sponge layer from

20° to 30° of latitude. The above interpolation and smoothing steps are repeated with the precipitation, cloud cover, and Levitus climatology to produce fluxes of heat and moisture over the rectangular basin.

The steady-forced model converges to an asymmetric mean state within 20 yr of run time. For the hypothesis-1 tests, we then apply idealized equatorially symmetric, annually varying winds as a small perturbation to the steady asymmetric winds. The small perturbation is generated by fitting an annual harmonic to the 2 years of monthly mean QuikSCAT wind stress and symmetrizing the winds about the equator. At each grid point and time, the symmetrized windfield is defined by

$$\begin{bmatrix} \tau'_{x,s}(x, y, t) \\ \tau'_{y,s}(x, y, t) \end{bmatrix} = 0.5\varepsilon \begin{bmatrix} \tau'_x(x, y, t) + \tau'_x(x, -y, t) \\ \tau'_y(x, y, t) + \tau'_y(x, -y, t) \end{bmatrix}. \quad (2)$$

In an effort to avoid contamination from terrestrial winds, the perturbation domain is defined to be 165°–240°E and 10°S–10°N. Outside of this domain, the perturbation winds are tapered by a Gaussian function to zero at the model boundaries in all directions. The decay scales chosen for the taper are 40° of longitude and 20° of latitude. The model is then run for 15 yr with this perturbation wind stress forcing, with several values of ε chosen to test the linearity of the system response, and the model solutions are analyzed from the years 31–35. The use of small values for ε avoids significant alteration of the asymmetry of the background currents.

a. SSH amplitude and zonal phase speed

When forced by symmetric, annually varying perturbation wind stress with $\varepsilon = 0.02$, the model with asymmetric background mean currents generates asymmetric Rossby waves (Fig. 7). The northern and southern maxima of SSH span nearly the entire Pacific in the TOPEX/Poseidon observations (upper-left panel, Fig. 2). The simulated northern and southern maxima of SSH are negligible east of 240°E (upper-left panel, Fig. 7), which is the direct result of choosing 240°E as the eastern boundary of the wind perturbation domain. Zonal averaging of the amplitudes between the western boundary (126°E) and the eastern edge of the perturbation domain (240°E) shows that the northern maximum along 4.7°N is 1.7 times the southern maximum along 5.2°S (upper-right panel, Fig. 7). The westward phase speeds of 52.9 ± 13.3 and 53.4 ± 13.3 cm s⁻¹ along the northern and southern maxima, respectively, are nearly equal. The SSH structure in Fig. 7 supports the hypothesis that the observed wave amplitude asymmetry is due to the asymmetry of the background mean flow. The equatorial symmetry of the model phase speeds, however, indicates that another mechanism is evidently responsible for the approximately 25% faster observed phase speeds in the north than in the south.

There are curious local maxima near 12°N/S in the model SSH amplitudes in the central Pacific. A similar peak is present along 12°N in the TOPEX/Poseidon observations (Fig. 2) and in the benchmark run (Figs. 5 and 6). The northern peak results from the superposition of local annual forcing with a traveling annual Rossby wave originating in the eastern Pacific (White 1977) and can be seen in x–t diagrams of model SSH (not shown here). The southern peak in the model SSH results from the symmetrized perturbation winds used here to force the model. The Gaussian tapering of wind stress used here to restrict the perturbation winds to the equatorial waveguide artificially enhances the wind stress curl poleward of 10° of latitude and provides intensified local forcing of this real feature. The intensity of the peak increases linearly as the magnitude of the perturbation (ε) increases. Experiments with different tapers (e.g., a linear taper) successfully eliminate the spurious amplification of these peaks, but this is not pursued further since our focus is on the structure of the variability within the equatorial waveguide between about 8°S and 8°N.

b. Vertical structure and modal decomposition

The existence of background currents alters the meridional structure of equatorial Rossby waves (Chelton et al. 2003; Fig. 7). To quantify the subsurface effects of the ECS on the Rossby waves, we construct the meridional and vertical (y, z) structures for zonal velocity which we interpret as representative of the first two shear-modified meridional Rossby wave modes for our hypothesis 1 simulation with $\varepsilon = 0.02$. Here the model zonal velocity is treated in terms of (y, s) space, where s is the vertical layer, and then converted to (y, z) space for graphical display.

We seek a separated representation of the zonal velocity annual signal (filtered as in section 2c) u, of the form

$$u(x, y, s, t) = B_{u,1}(x, t)F_{u,1}(y, s) + B_{u,2}(x, t)F_{u,2}(y, s),$$
$$(3)$$

where we specify the spatial modes $F_{u,i}(y, s)$ as

$$F_{u,i}(y, s) = u(x_0, y, s, t_i). \quad (4)$$

The temporally varying amplitudes $B_{u,i}(x, t)$ of these spatial modes are obtained by computing the linear regression of $u(x, y, s, t)$ onto the spatial structures $F_{u,1}(y, s)$ and $F_{u,2}(y, s)$, where the t_1 and t_2 in (4) represent times when the zonal velocity is dominated by modes 1 and 2, respectively, as described below.

The location x_0 is chosen to be 200.1°E in order to avoid the influence of TIWs in the eastern Pacific, and the times, t_1 and t_2, are chosen based on the temporal variability of the depth-averaged (layers 4–7) zonal velocity EOF 1 at 200.1°E, computed as in section 3 except for the hypothesis-1 simulation with $\varepsilon = 0.02$. The
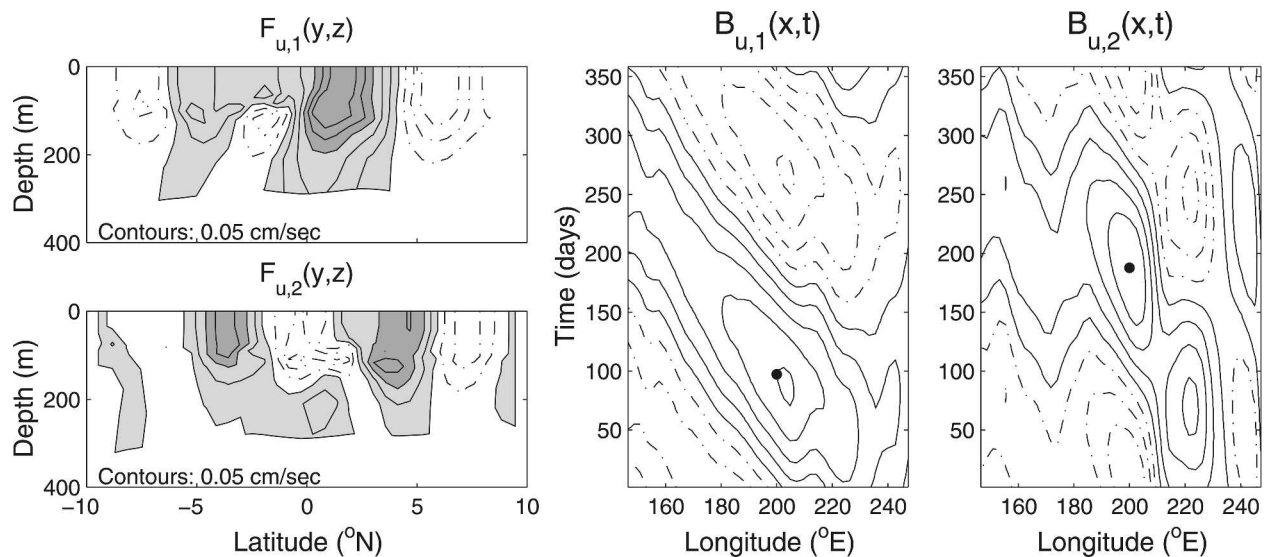
FIG. 8. (left) Structure functions (y, z) of the zonal velocity annual signal for modes 1 and 2 of the Gent–Cane model with rectangular basin forced with 2-yr mean zonal winds plus symmetric perturbation winds $(\varepsilon = 0.02)$. Regression coefficients as a function of longitude and time for (center) mode 1 and (right) mode 2, respectively, which demonstrate westward propagation. The contour interval is 0.25, dash–dot lines depict negative contours, and the dots indicate (x_0, t_1) and (x_0, t_2).

maximum in the EOF-1 amplitude time series occurs on day $t_1 = 99$, and the following zero crossing in this time series occurs on day $t_2 = 189$. Because the first zonal velocity EOF mode has the structure of meridional mode-1 Rossby wave modified by the model ECS (as in center panels of Fig. 6), the structure at t_2 should represent ECS modified meridional mode-2 structure.

As expected, (y, s) structures of the zonal velocity for t_1 and t_2 projected onto (y, z) space (left panels of Fig. 8) are latitudinally asymmetric with meridional structures in the upper layer that resemble modes 1 and 2 modified by asymmetric background currents (lower-right panel, Fig. 4). Except near 2°S, the vertical structures of both $F_{u,1}(y, z)$ and $F_{u,2}(y, z)$ indicate vertical mode-1 Rossby waves; near 2°S, the vertical structures are somewhat less clear, especially for $F_{u,1}(y, z)$.

The linear regression coefficients, $B_{u,1}(x, t)$ and $B_{u,2}(x, t)$ (center and right panels of Fig. 8) exhibit westward propagation with phase speeds on the order of 45 and 30 cm s^{-1} for modes 1 and 2, respectively. The westward phase speed found for $B_{u,1}(x, t)$ is consistent with the phase speed determined from SSH in section 4a. In the absence of an analytical representation of the subsurface effects of background currents on the Rossby waves in a nonlinear system, we have obtained empirically a separable structure for u with clear westward propagation.

c. Sensitivity to ε

To determine whether waves generated in the nonlinear Gent–Cane model behave linearly, we study the sensitivity of the hypothesis 1 experiments to the magnitude of the symmetric perturbation winds by running

the model with $\varepsilon = 0.01, 0.02, 0.05,$ and 0.10. The measures utilized to highlight the sensitivity of the model runs to ε include U_ε, the 5-yr model mean (years 31–35), depth-averaged (layers 1–7) zonal velocity along 141°W (Fig. 9), and the zonally averaged SSH amplitude maxima (between 126° and 240°E) and westward phase speeds along 4.7°N and 5.2°S (Fig. 10).

The extent to which nonlinearities in the Gent–Cane model are important can be inferred from the differences between U_ε and U_0, the depth-averaged zonal velocity in the absence of perturbation winds (upper panel, Fig. 9). As ε decreases, the difference between U_ε and U_0 decreases as expected (lower panel, Fig. 9). Though small, the latitudinal structure of $U_\varepsilon - U_0$ is asymmetric for all values of ε, evidence of weak nonlinear interactions between the asymmetric background mean circulation and the symmetric annually varying perturbation. The small differences between U_ε and U_0 relative to U_0 indicate that symmetric perturbations with ε as high as 0.10 are insufficient to significantly alter the asymmetry of the background mean flow and shear. Thus, the hypothesis-1 assumption of asymmetric background flow holds.

For linear waves, the amplitudes of the SSH maxima are expected to increase linearly as the magnitude of the perturbation forcing (ε) increases, and the phase speeds are not expected to change. The SSH maxima for the hypothesis-1 experiments (upper panel, Fig. 10) do increase linearly with increasing ε. The ratio of the northern maximum to the southern maximum is nearly a constant value, 1.6, essentially independent of ε. The westward phase speeds of about 53 cm s^{-1} along 4.7°N and 5.2°S are also independent of ε (lower panel, Fig.

Depth Averaged Velocity along 219.1°E (5 yr mean)
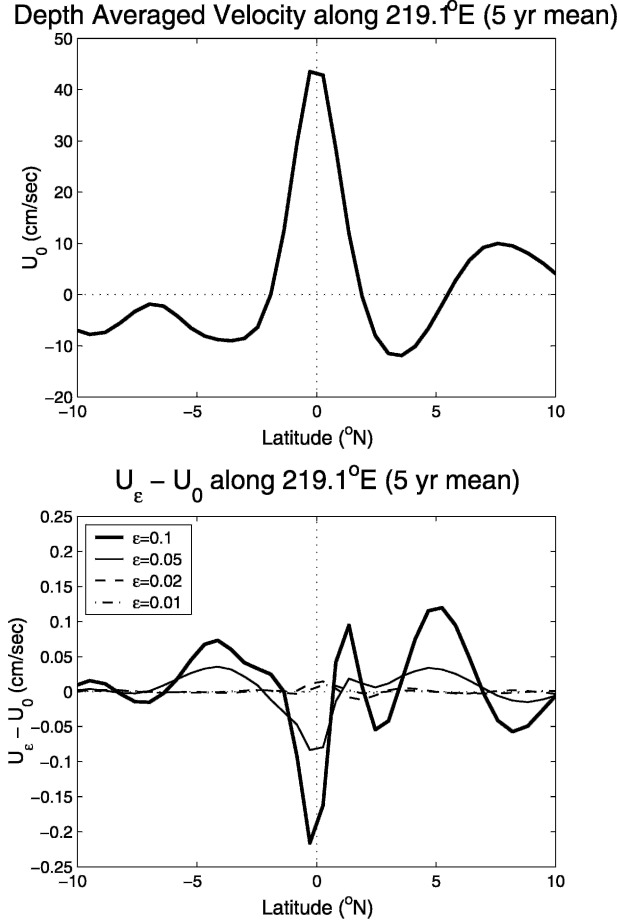

Uε – U0 along 219.1°E (5 yr mean)

FIG. 9. Dependence of the 5-yr model mean (years 31–35) depth-averaged (layers 1–7) zonal velocity, U_ε, along 219°E (141°W) on ε for the Gent–Cane model forced with 2-yr mean zonal wind plus symmetric perturbation winds. (top) Zero perturbation depth-averaged zonal velocity, U_0. (bottom) $U_\varepsilon - U_0$ for $\varepsilon = 0.01$ (dash–dot line), 0.02 (dashed line), 0.05 (thin solid line), and 0.10 (thick solid line).

Zonal Mean SSH Amplitude Dependence on ε
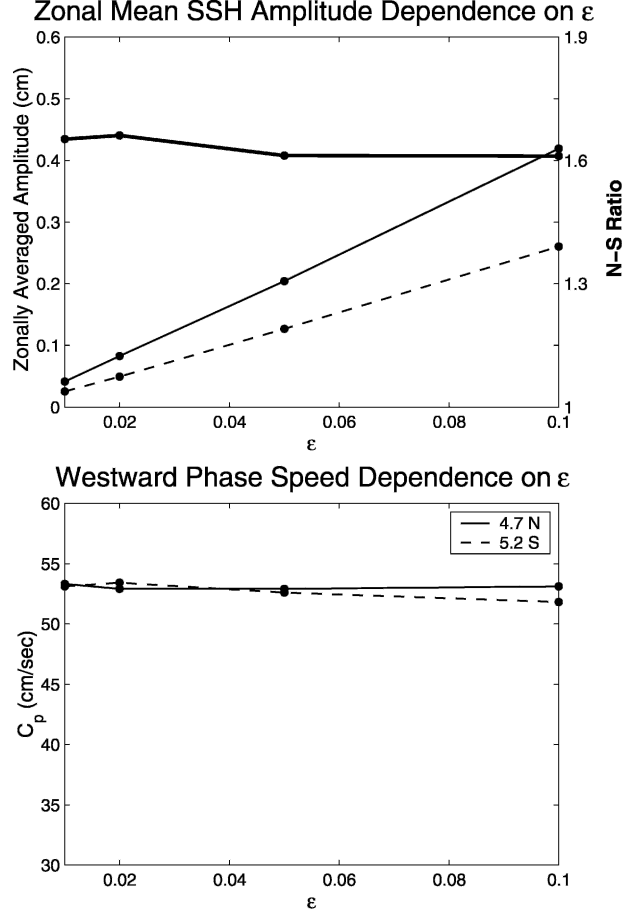

Westward Phase Speed Dependence on ε

FIG. 10. (top) The zonally averaged (126°–240°E) SSH amplitude and (bottom) westward phase speeds along 4.7°N (thin solid line) and 5.2°S (dashed line), and the ratio of the northern values to the southern values (thick solid line with right y-axis scale) as functions of the perturbation wind amplitude ε for the Gent–Cane model forced with 2-yr mean zonal wind plus symmetric perturbation winds. The smallest value of ε tested was 0.01.

10). The ratio of the northern phase speed to the southern phase speed is approximately 1.0 for all values of ε. The asymmetry of the Rossby wave SSH amplitudes and the symmetry of the estimated phase speeds are therefore robust features in this set of experiments where the background mean flow is asymmetric.

5. Hypothesis 2: Asymmetric wind forcing

In the second set of experiments, we perturb the model about a symmetrized background mean state. The goal is to produce a latitudinally symmetric mean circulation that possesses symmetrized versions of the general features of the Pacific Ocean. The background zonal wind stress is similar to that of (1) in section 4 but is symmetrized with respect to latitude such that

$$\bar{\tau}_s^x(x, y) = 0.5[\bar{\tau}^x(x, y) + \bar{\tau}^x(x, -y)]. \quad (5)$$

The heat and moisture fluxes used in section 4 are symmetrized with respect to latitude in the same manner. The model is run for 20 yr under these conditions, by which time it converges to a steady, symmetric mean state.

The time-varying wind stress perturbation in the model runs for testing hypothesis 2 consists of idealized equatorially asymmetric, annually varying winds generated by fitting an annual harmonic to the 2 years of QuikSCAT wind stress and allowing the winds to retain the observed asymmetric structure about the equator:

$$\begin{bmatrix} \tau'_{x,a}(x, y, t) \\ \tau'_{y,a}(x, y, t) \end{bmatrix} = \varepsilon \begin{bmatrix} \tau'_x(x, y, t) \\ \tau'_y(x, y, t) \end{bmatrix}. \quad (6)$$

The strength of the perturbation winds (ε), the domain over which the perturbation winds are applied, and the Gaussian taper outside of the domain are the same as in the previous numerical experiments de-
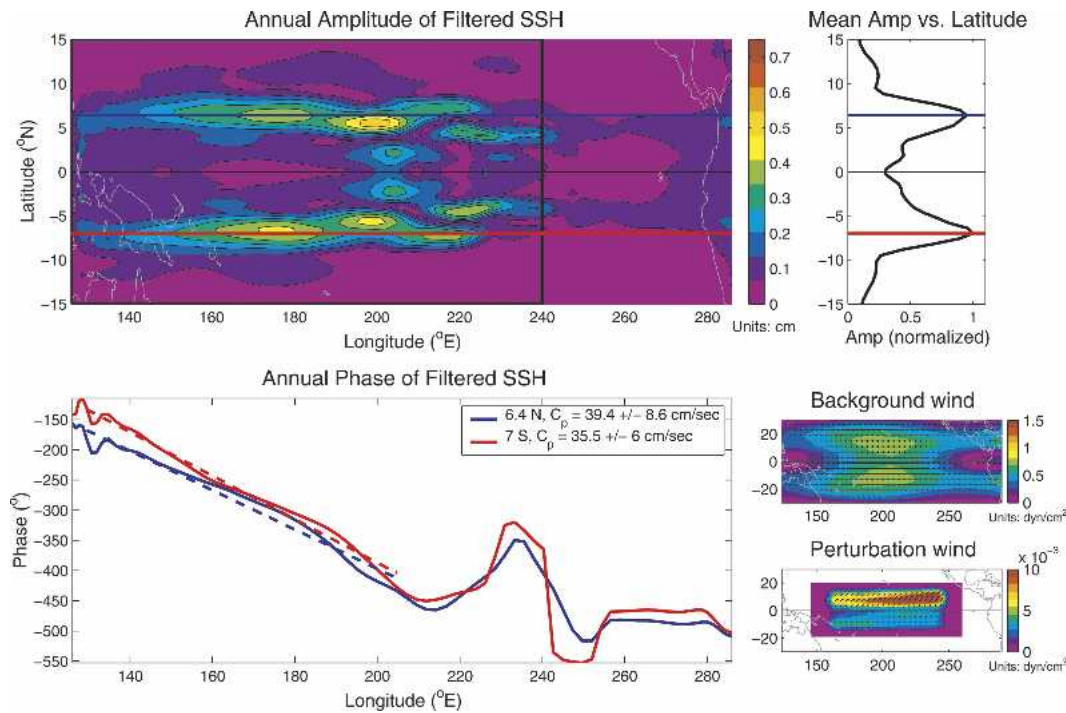
FIG. 11. Similar to Fig. 7, but SSH from the Gent–Cane model with a rectangular basin forced with symmetric 2-yr zonal mean wind plus asymmetric perturbation winds ($\varepsilon = 0.02$) derived from QuikSCAT wind stress as described in the text. Phase lines along 7.0°S and 6.4°N are shown in red and blue, respectively.

scribed in section 4. (Additional values of ε are included to resolve curious behavior near $\varepsilon = 0.05$ in section 5b.) The model is then run for an additional 15 yr with the perturbation wind stress forcing, and model solutions are analyzed from years 31 to 35.

a. SSH amplitude and zonal phase speed

The model forced by asymmetric annually varying perturbation winds about a symmetric mean state with $\varepsilon = 0.02$ generates essentially symmetric Rossby waves (Fig. 11). The zonally averaged (between 126° and 240°E) SSH maxima are along 6.4°N and 7.0°S, which differs from the 3.7°N/S maxima of classical theory (solid line, Fig. 1) but presents a nearly symmetric pattern about the equator. The EUC in the hypothesis-2 experiments (not shown) is slightly stronger than the EUC of the hypothesis-1 experiments, which is consistent with the shift of the SSH maxima from 4.7°N and 5.2°S to the higher latitudes of 6.4°N and 7.0°S (Philander 1979). The westward phase speeds of 39.4 ± 8.6 and 35.5 ± 6.0 cm s^{-1} along 6.4°N and 7.0°S, respectively, are somewhat smaller than those observed but are not significantly different on the two sides of the equator. This model run suggests that asymmetric wind forcing does not generate latitudinally asymmetric Rossby waves without an asymmetric background mean flow.

The 12°N peak previously described in section 4 (hypothesis 1) is again present and increases in strength as

the magnitude of the perturbation winds ε increases (see section 5b). Since the perturbation winds are not symmetrized for the model runs for testing hypothesis 2, there is no matching peak along 12°S.

b. Sensitivity to ε

The dependence of the hypothesis-2 numerical experiments on the magnitude of the asymmetric perturbation winds is explored by running the model with $\varepsilon = 0.01$, 0.02, 0.04, 0.05, 0.06, 0.08, and 0.10. We evaluate the linearity of the system response and observe the changes in the depth- and time-averaged zonal velocities as the value of ε increases.

In the hypothesis-1 experiments (section 4c), the background shear is strongly asymmetric and symmetric perturbations winds with ε as high as 0.10 are unable to significantly alter the asymmetry of the background currents (lower panel, Fig. 9). In this set of experiments, to test hypothesis 2, U_0 is latitudinally symmetric (upper panel, Fig. 12) and the latitudinal structure of $U_\varepsilon - U_0$ (lower panel, Fig. 12) remains nearly symmetric for $\varepsilon < 0.05$. For $\varepsilon \geq 0.05$, the mean flow becomes increasingly asymmetric and $U_\varepsilon - U_0$ does not vary linearly with ε.

In contrast to the results obtained in section 4c, the amplitudes of the SSH maxima do not increase monotonically beyond $\varepsilon = 0.04$ for this set of experiments (upper panel, Fig. 13). The latitudes of the zonally av-
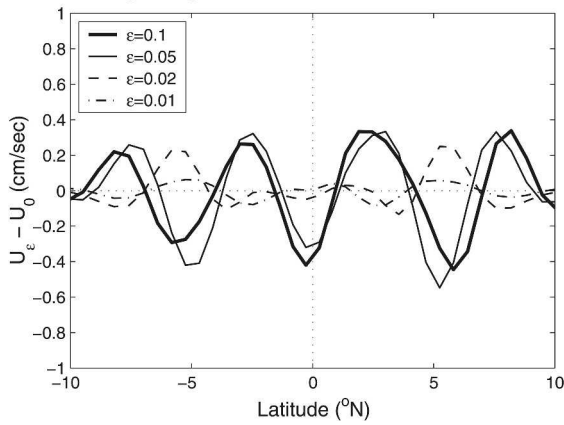
Depth Averaged Velocity along 219.1°E (5 yr mean)
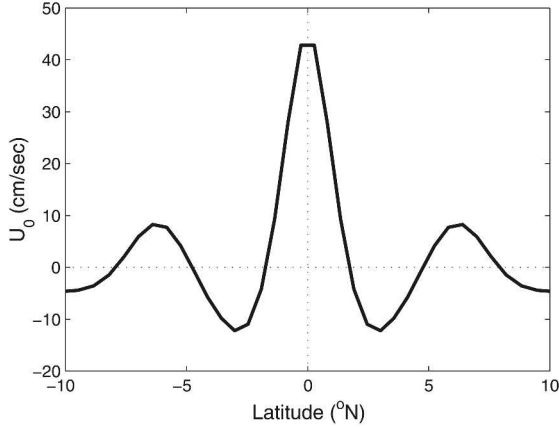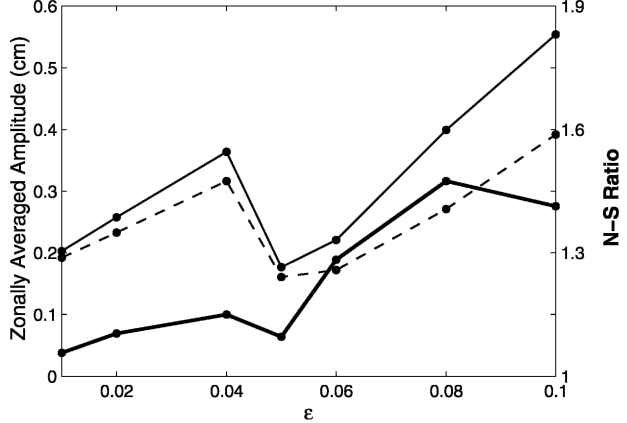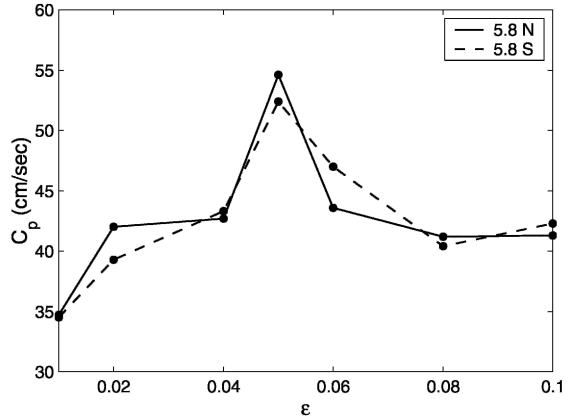

$U_\varepsilon - U_0$ along 219.1°E (5 yr mean)

FIG. 12. Similar to Fig. 9: dependence of the 5-yr model mean (years 31–35) depth-averaged (layers 1–7) zonal velocity, U_ε, along 219°E (141°W) on ε for the Gent–Cane model forced with symmetric mean plus asymmetric perturbation winds. (top) Zero perturbation depth-averaged zonal velocity, U_0. (bottom) $U_\varepsilon - U_0$ given $\varepsilon = 0.01$ (dash–dot line), 0.02 (dashed line), 0.05 (thin solid line), and 0.10 (thick solid line).

Zonal Mean SSH Amplitude Dependence on ε

Westward Phase Speed Dependence on ε

FIG. 13. Similar to Fig. 10: (top) zonally averaged SSH amplitude and (bottom) westward phase speeds along 5.8°N (thin solid line) and 5.8°S (dashed line), and the ratio of the northern values to the southern values (thick solid line with right y-axis scale) as functions of the perturbation wind amplitude ε for the Gent–Cane model forced with symmetric mean plus asymmetric perturbation winds. Additional values of ε ($\varepsilon = 0.04, 0.06,$ and 0.08) were tested.

eraged (between 126° and 240°E) SSH amplitude maxima range from 5.2° to 7.0°, depending on ε, and so we select a median latitude, 5.8°, to carry out the analysis. For $0.01 \leq \varepsilon \leq 0.05$, the ratios of the amplitudes of the northern and southern maxima are very close to 1. The northern maximum increases to approximately 1.3 times the southern maximum for $\varepsilon > 0.05$. The westward phase speeds along 5.8°N/S increase from 35 to 54 cm s^{-1} as ε increases from 0.01 to 0.05 but then decrease to 40 cm s^{-1} for $\varepsilon \geq 0.08$ (lower panel, Fig. 13). For all values of ε considered, the ratio of the northern phase speed to the southern phase speed is close to 1.0.

The near symmetry of the Rossby wave SSH amplitudes and the depth- and time-averaged zonal velocity are maintained for $\varepsilon < 0.05$. For $\varepsilon \geq 0.05$, the asymmetric wind perturbation becomes large enough to upset the underlying symmetry of the background flow

and thus generate significantly asymmetric Rossby waves, as apparent from the SSH amplitudes when $\varepsilon = 0.10$ (Fig. 14). The structure of the SSH amplitude under these conditions (upper-left panel, Fig. 14) differs from the observed structure as the simulated southern maximum extends farther into the central Pacific than is observed from TOPEX/Poseidon (upper-left panel, Fig. 2). This is probably due to the unrealistic and possibly unstable symmetric background circulation and the lack of coastlines (i.e., the rectangular basin in the model runs considered here).

In our hypothesis-2 experiments, we thus find that $\varepsilon \geq 0.05$ is sufficient to alter the symmetry of the background mean flow via nonlinear interactions. Consistent with the hypothesis-1 results, the asymmetrization of the hypothesis-2 mean flow for $\varepsilon \geq 0.05$ produces asymmetric Rossby waves.
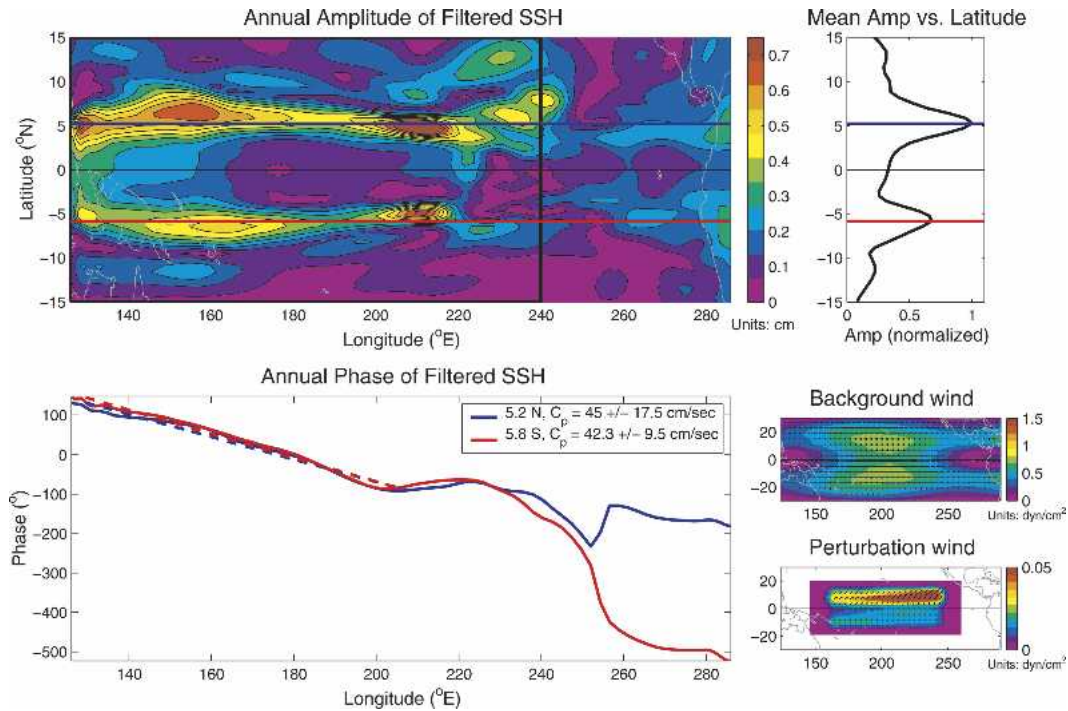
FIG. 14. Similar to Fig. 11, but for $\varepsilon = 0.10$. Phase lines along 5.8°S and 5.2°N are shown in red and blue, respectively.

6. Summary and conclusions

The Gent–Cane model was used in this study to test two potential mechanisms for the asymmetry of annual equatorial Rossby waves and the discrepancy between the predicted and observed westward phase speeds. The two mechanisms tested were asymmetry of the background mean currents (hypothesis 1) and asymmetric annually varying wind forcing (hypothesis 2). We considered rectangular basins to avoid introducing asymmetries due to coastline geometry.

The Gent–Cane model with asymmetric background mean currents perturbed by symmetric annually varying winds generated asymmetric annual equatorial Rossby waves with latitudinal structure similar to the observed asymmetry (Fig. 7), independent of the amplitude of the symmetric perturbation winds (Fig. 10). Vertical structure and modal decomposition were used to gain insight into the modification of the Rossby waves by the background ECS (Fig. 8). In the presence of asymmetric background currents, simulated waves were found to have a separable structure; that is, the annual deviations from the mean were well described by westward-propagating waves of the form given by (3) in section 4b. In lieu of analytical solutions, this provides a quantitative description of the subsurface effects of the ECS on the propagating waves.

The model with symmetric mean currents perturbed by asymmetric annually varying winds generated symmetric equatorial Rossby waves when the magnitude of the annually varying wind stress was sufficiently small ($\varepsilon < 0.05$) relative to the background wind stress (Figs. 11 and 13). Because this system behaves nonlinearly, asymmetric Rossby waves resulted when the magnitude of the asymmetric wind perturbation became sufficiently large ($\varepsilon \geq 0.05$), as shown in Figs. 13 and 14. For these larger values of ε, nonlinearity caused the 5-yr mean, depth-averaged zonal currents, U_ε, to deviate from the unperturbed symmetric background current, U_0 (lower panel, Fig. 12), and thus destroyed the symmetry of the mean circulation.

The model runs for testing hypothesis 2 thus indicate that asymmetric wind forcing in the absence of an asymmetric background mean ECS does not generate asymmetric Rossby waves. This is consistent with the results obtained by Kessler and McCreary (1993) from a linear model with $U_0 = 0$. Therefore, the numerical experiments in sections 4 and 5 demonstrate that the primary mechanism for the observed asymmetric latitudinal structure of equatorial Rossby waves is asymmetric meridional shears in the background flow (hypothesis 1). Asymmetric time-varying wind forcing serves as a secondary and weaker mechanism in the presence of an asymmetric ECS.

As in the observations, the model-derived westward phase speeds in the presence of nonzero background currents were slower than the theoretical phase speeds. Table 2 compares phase speeds derived from observations, analytic theory, and a subset of the numerical experiments conducted for this study. Hypothesis-1 ex-

periments succeeded in producing westward phase speeds with magnitudes similar to the observed phase speeds. In general, the hypothesis-2 experiments produced phase speeds that were significantly slower than observed. In both sets of experiments, the ratio of the phase speed along the northern maximum to the phase speed along the southern maximum was very nearly equal to 1.0. Phase speeds estimated from observations, however, found a northern phase speed that was slightly faster (by about 25%) than the southern phase speed.

Although the shear-modified eigensolutions in Chelton et al. (2003) yielded slower Rossby wave phase speeds than the classical theory, they were still about 20% faster than the observed phase speeds. The eigenvalue solutions for the phase speeds were calculated locally along selected longitudes. The resulting shear-modified phase speeds were therefore independent of latitude and oblivious to the effects of coastline geometry and time-varying wind forcing.

Since neither asymmetric background zonal currents (hypothesis 1) nor asymmetric wind forcing (hypothesis 2) succeeded at reproducing the observed Rossby wave phase speed asymmetry, the role of the asymmetric coastlines bounding the Pacific Ocean should be explored. The benchmark run forced by observed seasonal varying winds discussed in section 3 was able to capture a north–south phase speed difference of roughly 13%. Aside from the different time-varying wind forcing, the two significant differences in the benchmark run were the inclusion of coastline geometry and asymmetries in both the mean and time-varying wind forcing. Numerical experiments (not shown here) indicate that the combined asymmetry of the background and perturbation winds do not play a role in the phase speed asymmetry. In contrast, experiments with asymmetric background shear (lower-left panel in Fig. 4), realistic coastlines, and symmetric perturbations ε (also not shown here) produced phase speeds that were roughly 23% faster along 5.2°N than along 5.2°S (50.1 and 40.7 cm s^{-1}, respectively). Comparing these numbers with the model basin width X_E along each of those latitudes, we find that $X_{E,5.2N}$ is approximately 27% larger than $X_{E,5.2S}$ remarkably similar to the 23% phase speed differences. Annual Rossby wave phase speeds in the equatorial waveguide evidently depend on the width of the basin. A detailed analysis of the effect of coastline geometry on the ECS and the phase speeds of annual equatorial Rossby waves will be the focus of a future study.

REFERENCES

Chang, P., and S. G. H. Philander, 1989: Rossby wave packets in baroclinic mean currents. *Deep-Sea Res.,* **36,** 17–37.

Chelton, D. B., 2005: The impact of SST specification on ECMWF surface wind stress fields in the eastern tropical Pacific. *J. Climate,* **18,** 530–550.

——, R. A. de Szoeke, M. G. Schlax, K. El Naggar, and N. Siwertz, 1998: Geographical variability of the first baroclinic Rossby radius of deformation. *J. Phys. Oceanogr.,* **28,** 443–460.

——, and Coauthors, 2001: Observations of coupling between surface wind stress and sea surface temperature in the eastern tropical Pacific. *J. Climate,* **14,** 1479–1498.

——, M. G. Schlax, J. M. Lyman, and G. C. Johnson, 2003: Equatorially trapped waves in the presence of meridionally sheared baroclinic flow in the Pacific Ocean. *Progress in Oceanography,* Vol. 56, Pergamon, 323–380.

Chen, D., L. M. Rothstein, and A. J. Busalacchi, 1994a: A hybrid vertical mixing scheme and its application to tropical ocean models. *J. Phys. Oceanogr.,* **24,** 2156–2179.

——, A. J. Busalacchi, and L. M. Rothstein, 1994b: The roles of vertical mixing, solar radiation, and wind stress in a model simulation of the sea surface temperature seasonal cycle in the tropical Pacific Ocean. *J. Geophys. Res.,* **99,** 20 345–20 359.

Cox, M. D., 1980: Generation and propagation of 30-day waves in a numerical model of the Pacific. *J. Phys. Oceanogr.,* **10,** 1168–1186.

Delcroix, T., J. Picaut, and G. Eldin, 1991: Equatorial Kelvin and Rossby waves evidenced in the Pacific Ocean through *Geosat* sea level and surface current anomalies. *J. Geophys. Res.,* **96** (Suppl.), 3249–3262.

——, J.-P. Boulanger, F. Masia, and C. Menkes, 1994: Geosat-derived sea level and surface current anomalies in the equatorial Pacific during the 1986–1989 El Niño and La Niña. *J. Geophys. Res.,* **99,** 25 093–20 107.

Dewitte, B., and G. Reverdin, 2000: Vertically propagating annual and interannual variability in an OGCM simulation of the tropical Pacific Ocean in 1985–94. *J. Phys. Oceanogr.,* **30,** 1562–1581.

Ducet, N., P. Y. Le Traon, and G. Reverdin, 2000: Global high-resolution mapping of ocean circulation from TOPEX/Poseidon and *ERS-1* and *-2*. *J. Geophys. Res.,* **105,** 19 477–19 498.

Eriksen, C. C., M. B. Blumethal, S. P. Hayes, and P. Ripa, 1983: Wind-generated equatorial Kelvin waves observed across the Pacific Ocean. *J. Phys. Oceanogr.,* **13,** 1622–1640.

Freilich, M. H., D. G. Long, and M. W. Spencer, 1994: Sea Winds: A scanning scatterometer for ADEOS II—Science overview. *Proc. Int. Geoscience and Remote Sensing Symp.,* Vol. II, Pasadena, CA, IEEE, 960–963.

Fu, L.-L., J. Vazquez, and C. Perigaud, 1991: Fitting dynamic models to the *Geosat* sea level observations in the tropical Pacific ocean. Part I: A free wave model. *J. Phys. Oceanogr.,* **21,** 798–809.

Gent, P. R., and M. A. Cane, 1989: A reduced gravity, primitive equation model of the upper equatorial ocean. *J. Comput. Phy.,* **81,** 444–480.

Hackert, E. C., A. J. Busalacchi, and R. Murtugudde, 2001: A

wind comparison study using an ocean general circulation model for the 1997–1998 El Niño. *J. Geophys. Res.,* **106,** 2345–2362.

Johnson, G. C., B. M. Sloyan, W. S. Kessler, and K. E. McTaggart, 2002: Direct measurements of upper ocean currents and water properties across the tropical Pacific Ocean during the 1990s. *Progress in Oceanography,* Vol. 52, Pergamon, 31–61.

Kelly, K. A., and L. Thompson, 2002: Scatterometer winds explain damped Rossby waves. *Geophys. Res. Lett.,* **29,** 1991, doi:10.129/2002GL015595.

Kessler, W. S., 1990: Observations of long Rossby waves in the northern tropical Pacific. *J. Geophys. Res.,* **95,** 5183–5217.

——, and J. P. McCreary, 1993: The annual wind-driven Rossby wave in the subthermocline equatorial Pacific. *J. Phys. Oceanogr.,* **23,** 1192–1207.

——, L. M. Rothstein, and D. Chen, 1998: The annual cycle of SST in the eastern tropical Pacific, diagnosed in an ocean GCM. *J. Climate,* **11,** 777–799.

——, G. C. Johnson, and D. W. Moore, 2003: Sverdrup and nonlinear dynamics of the Pacific Equatorial Currents. *J. Phys. Oceanogr.,* **33,** 994–1008.

Kraus, E. B., and J. S. Turner, 1967: A one-dimensional model of the seasonal thermocline. Part II. The general theory and its consequences. *Tellus,* **19,** 98–105.

Levitus, S., 1982: *Climatological Atlas of the World Ocean.* National Oceanic and Atmospheric Administration, 173 pp.

Lukas, R., and E. Firing, 1985: The annual Rossby wave in the central equatorial Pacific Ocean. *J. Phys. Oceanogr.,* **15,** 55–67.

Matsuno, T., 1966: Quasi-geostrophic motions in the equatorial area. *J. Meteor. Soc. Japan,* **44,** 25–43.

Meyers, G., 1979: On the annual Rossby wave in the tropical North Pacific. *J. Phys. Oceanogr.,* **9,** 663–674.

Moore, D. W., 1968: Rossby waves in an equatorial ocean. Ph.D. dissertation, Harvard University, Cambridge, MA, 207 pp.

——, and S. G. H. Philander, 1977: Modeling of the tropical oceanic circulation. *The Sea,* E. D. Goldberg et al., Eds., Vol. 6, Wiley-Interscience, 319–361.

Murtugudde, R., and A. J. Busalacchi, 1998: Salinity effects in a tropical ocean model. *J. Geophys. Res.,* **103,** 3283–3300.

——, R. Seager, and A. J. Busalacchi, 1996: Simulation of the tropical oceans with an ocean GCM coupled to an atmospheric mixed-layer model. *J. Climate,* **9,** 1795–1815.

——, J. Beauchamp, C. R. McClain, M. Lewis, and A. J. Busalacchi, 2002: Effects of penetrative radiation on the upper tropical ocean circulation. *J. Climate,* **15,** 470–486.

Philander, S. G. H., 1978: Instabilities of zonal equatorial currents, Part 2. *J. Geophys. Res.,* **83,** 3679–3682.

——, 1979: Equatorial waves in the presence of the equatorial undercurrent. *J. Phys. Oceanogr.,* **9,** 254–262.

Price, J. F., R. A. Weller, and R. Pinkel, 1986: Diurnal cycling: Observations and models of the upper ocean response to diurnal heating, cooling, and wind mixing. *J. Geophys. Res.,* **91,** 8411–8427.

Qiao, L., and R. H. Weisberg, 1995: Tropical instability wave kinematics: Observations from the Tropical Instability Wave Experiment. *J. Geophys. Res.,* **100,** 8677–8693.

Rossow, W. B., and R. A. Schiffer, 1991: ISCCP cloud data products. *Bull. Amer. Meteor. Soc.,* **72,** 2–20.

Schlax, M. G., and D. B. Chelton, 1992: Frequency domain diagnostics for linear smoothers. *J. Amer. Stat. Assoc.,* **87,** 1070–1081.

Seager, R., S. E. Zebiak, and M. A. Cane, 1988: A model of the tropical Pacific sea surface temperature climatology. *J. Geophys. Res.,* **93,** 1265–1280.

Susanto, R. D., Q. Zheng, and X.-H. Yan, 1998: Complex singular value decomposition analysis of equatorial waves in the Pacific observed by TOPEX/Poseidon altimeter. *J. Atmos. Oceanic Technol.,* **15,** 764–774.

Verron, J., L. Gourdeau, D. T. Pham, R. Murtugudde, and A. J. Busalacchi, 1999: An extended Kalman filter to assimilate satellite altimeter data into a nonlinear numerical model of the tropical Pacific Ocean: Method and validation. *J. Geophys. Res.,* **104,** 5441–5458.

White, W. B., 1977: Annual forcing of baroclinic long waves in the tropical North Pacific Ocean. *J. Phys. Oceanogr.,* **7,** 50–61.

Yu, X., and M. J. McPhaden, 1999: Seasonal variability in the equatorial Pacific. *J. Phys. Oceanogr.,* **29,** 925–947.

Zheng, Q., X.-H. Yan, C.-R. Ho, and C.-K. Tai, 1994: The effects of shear flow on propagation of Rossby waves in the equatorial oceans. *J. Phys. Oceanogr.,* **24,** 1680–1686.